THE JOURNAL OF PHYSICAL CHEMISTRY C

pubs.acs.org/JPCC Article

Heterogeneous Surface Growth and Gelation of Cement Hydrates

Abhay Goyal, Katerina Ioannidou, Christopher Tiede, Pierre Levitz, Roland J.-M. Pellenq, and Emanuela Del Gado*

Cite This: J. Phys. Chem. C 2020, 124, 15500−15510 Read Online

ACCESS | Metrics & More | Article Recommendations | Supporting Information

ABSTRACT: During cement hydration, C−S−H nanoparticles precipitate and form a porous and heterogeneous gel that glues together the hardened product. C−S−H nucleation and growth are driven by dissolution of the cement grains, posing the question of how cement grain surfaces induce spatial heterogeneities in the formation of C−S−H and affect the overall microstructure of the final gel. We develop a model to examine the link between these spatial gradients in C−S−H density and the time-evolving effective interactions between the nanoparticles. Using a combination of molecular dynamics and Monte Carlo simulations, we generate the 3D microstructure of the C−S−H gel. The gel network is analyzed in terms of percolation, internal stresses, and anisotropy, and we find that all of these are affected by the heterogeneous C−S−H growth. Further analysis of the pore structure encompassed by the C−S−H networks shows that the pore size distributions and the tortuosity of the pore space show spatial gradients and anisotropy induced by the cement grain surfaces. Specific features in the effective interactions that emerge during hydration are, however, observed to limit the anisotropies in the structure. Finally, the scattering intensity and specific surface area are computed from the simulations in order to connect to the experimental methods of probing the cement microstructure.

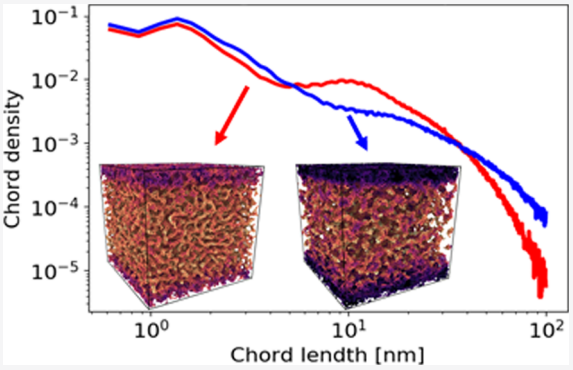

INTRODUCTION

It is well known that soft materials such as gels are formed under nonequilibrium conditions, and these conditions can have drastic effects on the final mechanical and morphological properties of the material. This is certainly the case for C−S−H (calcium−silicate−hydrate) gels formed during cement hydration. While cement is usually not thought of in the context of soft matter, its mechanical properties depend on this C−S−H "glue" which binds together the other hydration products.[1−3] During the setting process, C−S−H precipitates and aggregates into a gel which becomes denser and stiffer over time. It forms a complex pore structure and develops significant spatial heterogeneities.[4,5] These morphological features span from nano to microscales, making cement a truly multiscale material that is challenging to fully characterize.

Understanding the physical and chemical processes underlying cement hydration is of immense practical importance. Concrete is the most widely used, synthetic construction material, and cement is its main binding agent. The production of cement accounts for about 8% of global anthropogenic carbon dioxide emissions.[6] The intelligent design of new, greener cements is a pathway to greatly reduce those emissions, but this goal is hindered by an incomplete understanding of what makes the existing cement work as it does.[7] The complex hydration kinetics makes it challenging to fully understand the mechanisms that cause cement to set and how the final mechanical properties develop.[8−10] Despite the challenges, many recent studies have made inroads into developing such an understanding.

Rheology and specific surface area measurements tell us about the development of mechanical strength and porosity during setting.[4,11,12] This is driven by the formation of C−S−H, which precipitates as nanoparticles of size ≈5 nm,[1,13] and advances in nano-indentation techniques have enabled new insights into this nanoscale origin of the macroscopic mechanical properties.[14,15] However, several aspects of how the larger-scale morphology and mechanics of the material emerge from its nanoscale components need further investigation.

The combination of reaction kinetics driving the nucleation and growth of C−S−H particles[16,17] with changing effective interactions[18,19] drives the nonequilibrium formation of the C−S−H gel. This pathway has a clear effect on the microstructure, which shows strong spatial gradients and

Received: April 2, 2020
Revised: June 1, 2020
Published: June 16, 2020

https://dx.doi.org/10.1021/acs.jpcc.0c02944
J. Phys. Chem. C 2020, 124, 15500−15510

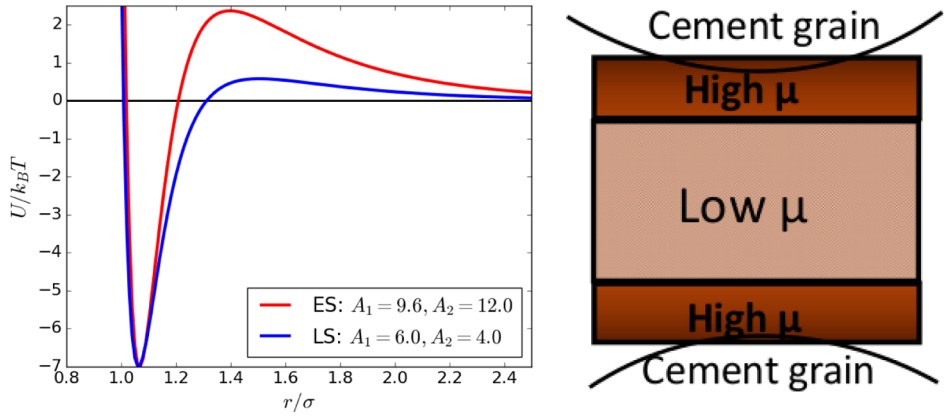

Figure 1. Left: We use two sets of parameters A_1, A_2 to consider different repulsive strengths. These are labeled ES and LS corresponding to a high and low repulsive barrier present in early and late stages of the cement setting. Right: A schematic of the variation of μ across our system. By considering a simulation volume between two cement grains, we introduce a spatial gradient in the hydration and the precipitation of C−S−H nanoparticles. The cement grain surface is not included explicitly, but rather through an effect on the local μ, turning it into a spatially varying quantity.

anisotropy, and it is in this context that the we need to understand the development of C−S−H morphology during hydration. To do so, one important question to answer is how exactly the way C−S−H forms affects its final properties. Another is how the changing interactions couple to the nonuniform C−S−H precipitation.

We use a mesoscale model to answer these questions, expanding on work which has had success in understanding the role of the changing interaction[20] and their effects on the hardened paste.[21] Specifically, we implement a spatial gradient in the C−S−H precipitation corresponding to the nucleation of C−S−H at cement grain surfaces. Using a wide range of computational analysis tools, we then characterize the C−S−H network, pore structure, internal stresses, and more. This gives insight into the effect of heterogeneous C−S−H growth mechanisms on the overall microstructure, but it also demonstrates how this effect is enhanced or limited by the features of the interaction potential. In particular, noncontact repulsion, which is present in the early stages of hydration, can limit the density gradients and anisotropy of the C−S−H gel, forming a percolated, porous network at low volume fractions. These results explain the surprising robustness of the C−S−H gel against phase separation induced by density gradients and against the formation of a dense C−S−H layer at the cement grain surface that blocks further reaction. Understanding the role of the interaction during the heterogeneous formation of the C−S−H gel is an important step toward designing new cementitious materials.

METHODS

In our model, C−S−H nanoparticles are coarse-grained and treated as spherical particles of a fixed size. An effective interaction potential is prescribed to these particles that includes the net interactions mediated using the solvent. The physics behind these interactions is a complex problem in itself. It has been studied extensively via both experiments and simulation.[18,19,22−26] The forces at play emerge from the fluctuations of the electrolyte solution confined between the highly charged C−S−H surfaces. While we do not include the solvent and counterions explicitly in the model here, it is the correlations between these species that give rise to strongly attractive noncontact forces between C−S−H nanoparticles. These correlations are highly dependent on ion concentrations and pH,[18] so the overall interactions change over time as the continued dissolution of cement alters the solution chemistry.

For simplicity, we consider fixed forms for the effective interaction during precipitation but investigate two different forms corresponding to different hydration times. Strikingly, the experiments show that the repulsive barrier decreases in height, eventually disappearing altogether, during hydration. Potentials with competing attraction and repulsion are known to exhibit complex phase diagrams,[27,28] and we focus our investigation on the effects of a change in the repulsive barrier height. To do so, we assume a generic model for the interaction potential that allows independent control of the width/height of the attractive well and repulsive barrier

$$\frac{U(r)}{\varepsilon} = A_1\left[\left(\frac{\sigma}{r}\right)^{2\gamma} - \left(\frac{\sigma}{r}\right)^{\gamma}\right] + A_2\frac{e^{-\kappa r}}{r} \quad (1)$$

where A_1 and A_2 are constants, σ and ε are the length and energy scales (discussed further in next section), respectively, and κ is the inverse Debye screening length. Considering the fact that these interactions were observed to be very short-ranged and that range did not significantly vary with pH in the experiments,[18] we fix $\gamma = 12$ and $\kappa = 0.5\sigma$. The ratio of A_1/A_2 sets the relative strength of attraction and repulsion, and we vary these so that the depth of the attractive well is fixed and only the repulsive barrier height changes for the two interaction potentials considered: ES and LS, corresponding to early and later stages of cement hydration (Figure 1, left). The ES potential exhibits a stronger repulsive barrier with $A_1 = 9.6$ and $A_2 = 12$, while the LS exhibits reduced repulsion but a similar attractive well with $A_1 = 6$ and $A_2 = 4$. The depth of the attractive well (set by choosing a temperature of $k_BT = 0.15\varepsilon$) is such that aggregation is energetically favored but the dynamics can be studied over a reasonable simulation time. Additionally, it sets the barrier height to be $>2k_BT$ for the ES potential but $<k_BT$ for the LS. With these choices, the maximum force (obtained from dU/dr, taking the particle size to be $\sigma = 5$ nm and the potential well depth $\varepsilon \approx 7k_BT$) is comparable to the values obtained from atomic force microscopy measurements for low lime concentrations.[18]

In the physical system, C−S−H does not exist in equilibrium conditions. In fact, as the reaction proceeds,

https://dx.doi.org/10.1021/acs.jpcc.0c02944
J. Phys. Chem. C 2020, 124, 15500−15510

more and more C−S−H is created from the combination of ions and water.[9] These species are not included explicitly in our model, but we mimic this precipitation via a grand canonical Monte Carlo (GCMC) process, where particles are inserted and deleted with a probability given by the metropolis Monte Carlo scheme[29]

$$P_{\mathrm{ins/del}} \propto \min[1, e^{\pm\beta(\mu_{\mathrm{exc}} - \Delta U)}] \quad (2)$$

where $\beta = \frac{1}{k_B T}$, k_B is the Boltzmann constant, T is the temperature, μ_{exc} is the excess chemical potential, and ΔU is the total change in the energy upon inserting/deleting a particle. In a closed system, μ_{exc} is associated with all the interactions between particles and depends on the density and phase equilibria.

During cement hydration, the dissolution of cement grains increases the overall concentration of ions in solution, and when saturated, they combine to form a C−S−H molecule.[9] As we have coarse-grained out these degrees of freedom, the usual equilibrium chemical potential is not sufficient to describe this. Instead, we consider that the background chemistry has an effect of producing a net free energy gain with the creation of C−S−H.

With this assumption in mind, we take μ_{exc} to have two components

$$\mu_{\mathrm{exc}} = \mu_{\mathrm{interaction}} + \mu_{\mathrm{chemical}} \quad (3)$$

The interaction term is the usual μ_{exc},[29] while the chemical term represents the free energy gain of calcium, silicon, oxygen, and hydrogen coming together to form a C−S−H nanoparticle. While the equilibrium value of the first term can be computed (and indeed, it has, e.g., in refs 20 and 30), this chemical term is difficult to estimate. Considering that densification does not stop during cement hydration,[17] previous studies have used a value of μ_{exc} that favors insertion.[31]

Here, our scenario is different because we want C−S−H precipitation to vary spatially. There is a tendency for C−S−H to grow at the surface of cement grains or other nucleation sites.[16,17] If we consider our simulation box to be part of a pore between two cement grains (Figure 1, right), the hydration of the cement occurs near the edges of the box, as, primarily, does the precipitation of new C−S−H nanoparticles. To implement this, we consider $\mu_{\mathrm{exc}}(z)$ to be a quantity that depends on the position. Near the edges, a higher μ_{exc} will favor insertion, while far from the cement grains, a lower μ_{exc} will discourage insertion unless it is close to existing particles.

This GCMC process is combined with molecular dynamics (MD) of the C−S−H particles. Because of this coupling, the system exists in a non-equilibrium state where the kinetics of the reaction (mimiced by GCMC) affect the morphology of the system that evolve in time through MD. The rate R, which is the ratio of GCMC exchanges to MD steps, can be thought of as setting how fast C−S−H particle creation occurs. When R is very high or very low, the behavior of the system would be essentially dictated by either the precipitation kinetics (GCMC) or by the dynamical aggregation (MD). However, when $R \sim O(1)$, we are in a situation where the C−S−H precipitation and the particle dynamics interfere with each other to determine the gel morphology.

Simulation Details. We use m as the unit mass, σ as the unit length, and ε as the unit energy, which defines a unit time $\tau = \sqrt{\frac{m\sigma^2}{\varepsilon}}$. The simulation volume is a periodic cubic box of side length $L = 49.2\sigma$, in which we perform MD in an *NVT* ensemble with a Nosé−Hoover thermostat[29] at temperature $k_B T = 0.15\varepsilon$, which is comparable to room temperature when the interaction strength is calibrated to a modulus of 20 MPa for a C−S−H gel at early hydration times.[20] We solve the Newtonian equations of motion using the velocity Verlet algorithm with a time step of 0.0025τ. The GCMC and MD simulations here are done using LAMMPS.[32]

For GCMC exchanges, the simulation box is split into three regions along the z-axis. The top and bottom slices are high μ regions of thickness 5σ. In the case of ES (see Figure 1), we assign $\mu_{\mathrm{ES}} = 6\varepsilon$, while for the LS case, we set $\mu_{\mathrm{LS}} = 1.5\varepsilon$. The middle region has thickness 40σ and lower values of $\mu_{\mathrm{ES}} = -1\varepsilon$ and $\mu_{\mathrm{LS}} = -1.5\varepsilon$, respectively. These values have been calibrated so that insertion is always preferred in the edge regions, and in the middle regions, it can only happen near existing clusters.

In the simulations, the MD and GCMC parts are connected through the rate parameter R. This is the ratio of the number of GCMC exchanges to the number of MD time steps, and previous studies have found that varying R over the range of $R = 0.2-R = 4$ can change the densification.[31] At high R, more GCMC insertions/deletions are attempted, and this drives the system further from the equilibrium behavior associated with the interaction potential. We focus on a relatively high value of $R = 4$—where the thermodynamics of the system, dictated by the interactions, matters less—in order to investigate whether, even in these conditions, we could see a coupling between the spatial gradient and the specific interaction potential. This rate corresponds to 400 GCMC exchanges attempted every 100 MD steps, with a variable but approximately even split of 200 insertions/deletions each for every GCMC cycle. As we run the MD and GCMC, particles are inserted into the initially empty simulation box, and simulations are run until $N \approx 57{,}000$: corresponding to a volume fraction of $\phi = 0.25$. Here, ϕ is estimated considering spheres of diameter σ and hence computed as $\phi = \frac{N\pi\sigma^3}{6L^3}$. The whole simulations require approximately 10^6 MD steps, with variations that depend on the interaction potential. The MD time can be converted into real time (hydration time in the experiments) using the argument developed in ref 27, which indicates that $t_{\mathrm{exp}} \propto \log t_{\mathrm{sim}}$.[31]

RESULTS AND DISCUSSION

Using the microscopic information obtained from simulations, we analyze the structural and morphological features of the C−S−H gel. First, we examine how the precipitation of C−S−H leads to the formation of a percolating network and the buildup of internal stresses. Next, the consequences of this structure in terms of the size of pores and diffusion within them are investigated. Finally, we characterize the specific surface area and scattering intensity in order to make a connection with common experimental methods of characterizing the cement microstructure. The results for the percolation and stresses are presented in reduced units (m, σ, ε, τ, and unit pressure ε/σ^3). For the sections on porosity, specific surface area, and scattering, we convert to real units by setting $\sigma = 5$ nm to give a sense of the physical scale.

Percolation and Stresses. The choice of using a grand canonical ensemble allows the insertion of particles to occur at

https://dx.doi.org/10.1021/acs.jpcc.0c02944
J. Phys. Chem. C 2020, 124, 15500−15510

a nonuniform rate in a way that depends on the state of the system. As seen in Figure 2, the total volume fraction ϕ starts to increase more rapidly as particles are inserted—until ϕ saturates because of increasing density and steric repulsion between particles.

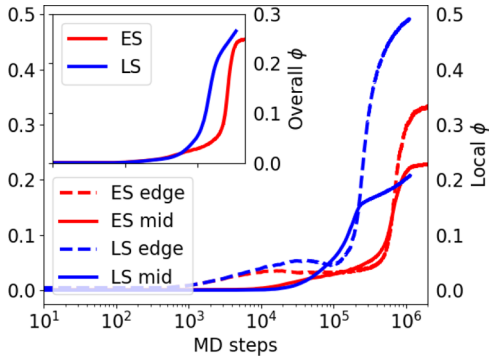

Figure 2. Variation of total and local (edge, middle) ϕ as the simulations progress. With LS interactions, the nonuniform μ leads to a much larger local ϕ difference between the edge and middle regions. The formation of a locally dense, crystalline (see the Supporting Information) layer near the cement grain surface is consistent with observations of the inner product or high-density C−S−H.[33,34]

Figure 2 also shows local ϕ in the edge and middle regions, defined as the 5σ thick high μ regions and the 39.2σ thick low μ region, respectively. Because of the diffusion of particles from the edge, the middle region actually becomes denser than the edge for a period, starting around $t = 10^5$ MD steps, consistent with observations of nano C−S−H seeds in the solution at early hydration times.[35] This reversal ends around ϕ = 15% when the edge ϕ starts to increase rapidly. For LS, this also corresponds to a sudden decrease in $d\phi/dt$ in the middle, as the dense structure at the edge limits diffusion. For ES, the increased growth rate at the edge is correlated with an increased growth rate in the middle. This holds until $\phi \approx 22\%$, when the deletions in the low μ regions balance the diffusion from the edge region.

We see a morphological difference between the two regions which becomes increasingly pronounced as more particles are inserted. Figure 3 shows that particles at the edge tend to be more clustered and densely packed. In these snapshots, at ϕ = 25%, simulations with both potentials show the formation of a

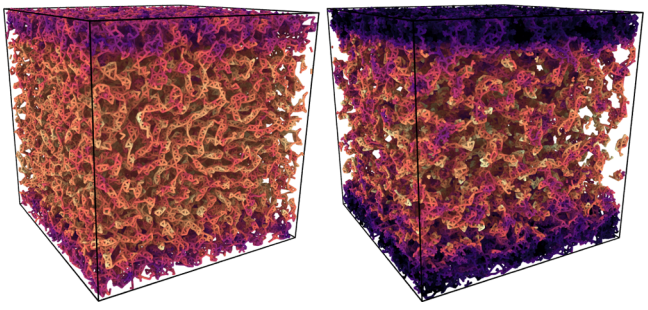

Figure 3. Simulation snapshots, with overall volume fraction ϕ = 25%, showing the microstructure for the ES potential (left) and LS potential (right). Color indicates the local density, with darker purple regions indicating many neighboring particles, and we see a high degree of anisotropy in the gel network which is dependent on the interaction potential.

percolated, system-spanning cluster. During the simulation, as ϕ increases, clusters grow and aggregate into a connected structure, and these morphological changes also couple back to how quickly and uniformly—or not—ϕ increases. While the C−S−H clusters eventually percolate in both cases, the way that structure forms and its final morphology are quite different.

To begin examining this process quantitatively, we group particles into clusters by defining a bonding distance, r_b. We use $r_b = 1.1\sigma$ here, corresponding to a bond distance such that two particles are near the minimum of the interaction potential, after having confirmed that varying r_b around this value does not change our results. It is to be noted that these bonds and clusters are defined solely by instantaneous distance, but because of the interaction strength chosen ($k_BT = 0.15\varepsilon$), they correspond to C−S−H particles that adhere to each other and do not continuously break and reform over time. Cluster percolation is defined as the formation of a cluster which spans the simulation box in x, y, and z directions. Figure 4 shows the percolation probability, that is, the fraction

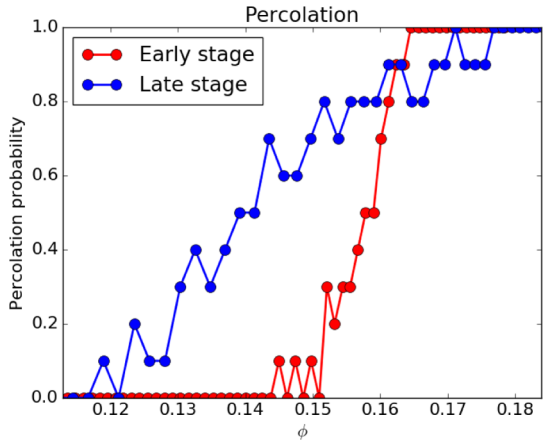

Figure 4. Geometric percolation probability as a function of ϕ. The particles are clustered according to a distance cutoff of 1.1σ. A cluster is considered percolating if it spans the system in x, y, and z directions. This says nothing about the persistence or rigidity of the percolating cluster and is a geometric definition rather than a mechanical one.

of independently generated systems that formed, in the same conditions of precipitation rate R, interaction strength ε, and volume fraction ϕ, a percolating connected structure. We gathered statistics from 10 independent samples for each potential. We see that, for ES, the percolation transition is more sharply defined, that is, it happens over a narrow range of ϕ. On the other hand, with LS there is a 6% volume fraction difference between the first occurrence of a percolating cluster and 100% percolation. Interestingly, the percolation seems to correspond with the density cross-over seen in Figure 2 at ϕ = 15% (where the local ϕ at the edge starts to rapidly increase over that in the middle). This suggests that the percolating cluster limits particle diffusion from the edge to the middle—especially for the LS potential.

In order to understand the mechanical implications of this percolation, we looked at the buildup of internal stresses within the material. Using the virial formulation of the stress tensor, one can define a coarse-grained local stress tensor.[36] To focus our analysis on the stresses associated with particle interactions

https://dx.doi.org/10.1021/acs.jpcc.0c02944
J. Phys. Chem. C 2020, 124, 15500−15510

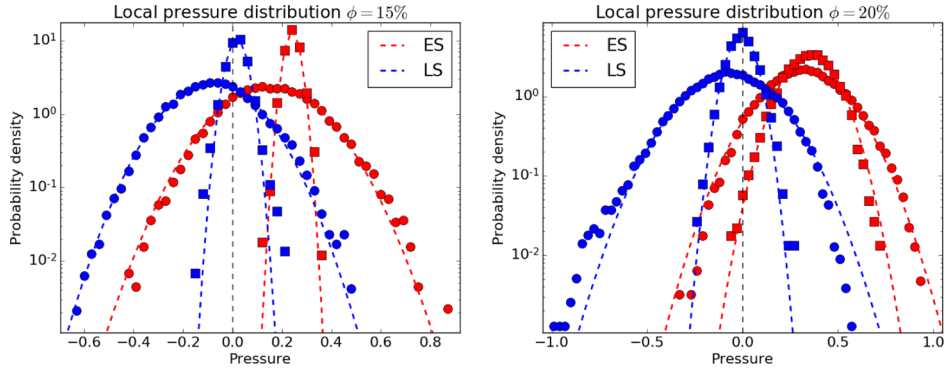

Figure 5. Distributions of local pressure at the edge (circle symbols) and center (square symbols). Gaussian fits are also plotted as dashed lines.

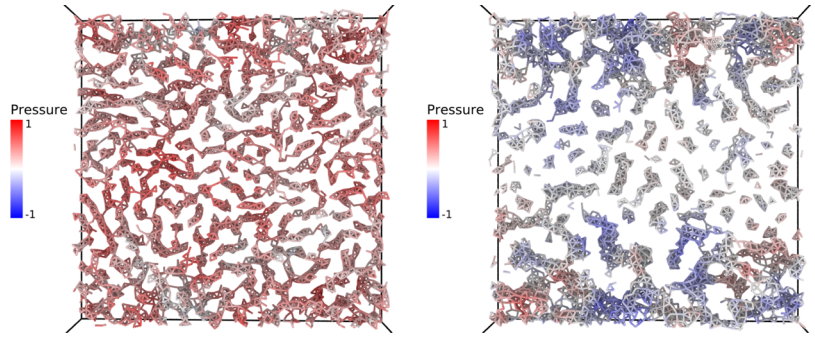

Figure 6. Thin (5σ) slice of our system at ϕ = 20% for ES (left) and LS (right). The coloring corresponds to the local pressure, with red being positive pressure, that is, parts under compression—and blue being negative pressure.

rather than thermal motion, we neglect the kinetic term and obtain

$$\sigma_{\alpha\beta} = -\frac{1}{V_{cg}} \sum_{i \epsilon V_{cg}} \sum_{j \neq i} \frac{1}{2} F_{\alpha}^{ij} r_{\beta}^{ij} \tag{4}$$

where α and β indicate the vector components, while i and j are summed over individual particles. Taking the trace of this gives us a local pressure which describes the forces a particle experiences and converges to the total pressure if we expand the coarse-graining volume, V_{cg}. For the results presented, we use $V_{cg} = \frac{4}{3}\pi r_c^3$, where r_c is the cutoff of the potential. Small variations of V_{cg} do not produce any qualitative differences.

Figure 5 shows the local pressure distributions for two values of ϕ in the edge and middle regions. They are plotted with Gaussian fit lines and show fairly normal distributions within each region. Around the percolation transition at ϕ = 15%, we see that ES and LS have similar distributions, but they are shifted because of the extra repulsion in ES. In both cases, there is a sharply defined value in the middle region, while the edges have a wider spread. Because the local ϕ in each region is roughly the same (see Figure 2), it is interesting that there is such a difference in the stress distributions, indicating that the two regions arrived at ϕ = 15% through different paths, which, in turn, modified the local morphology and stresses.

As we add particles and go to ϕ = 20%, the stresses in the ES case become more uniform across the simulation box. The center distribution widens and the peak of the edge distribution shifts. Once the connected structure percolates, the stresses can be transmitted between regions, and this serves as a mechanism to reduce the initial heterogeneities introduced by the chemical potential gradient. In contrast, the LS samples maintain the extreme differences in edge versus center distributions, indicating that they are not effectively connected to allow for stress redistribution. The geometric percolation of a cluster is enough to reduce the diffusion but not necessarily to transmit stresses, which suggests that the ES interactions are crucial to give the product an early mechanical response, as experiments have seen for cement mixtures.[11]

In Figure 6, we show snapshots from our simulations at ϕ = 20%, color coded according to local pressure. As one would expect from the stress distributions, the system snapshots show stresses that are more uniformly distributed for ES. In addition, there is no pronounced morphological difference between the edge and center regions. For LS, there is a clear distinction with most stressed areas lying on the edge of the system, which also corresponds to local structures that clearly differ from the edge to the middle (see the Supporting Information for more on local ordering).

The heterogeneities in density, stresses, and local packing present with the LS potential arise because of the spatial gradient in chemical potential μ and are coupled to the anisotropy that develops in the underlying network topology. In a quantitative sense, this can be probed by considering a random walk on the network graph constructed from the bonds in structures analyzed so far. The corresponding mean squared displacement (MSD_g) is plotted in Figure 7 as a function of the number of steps taken along the graph. The x and y directions are expected to be symmetric in a statistical sense, and unsurprisingly, the MSD_g along those directions is equal. On the other hand, the z direction—the direction of the spatial μ gradient—is set up to be distinct from the others, and we have shown that there are clear heterogeneities along this direction. These have a clear effect on the network graph as the z displacement differs from x and y for both ES and LS potentials. Notably, like the other measured properties, this

https://dx.doi.org/10.1021/acs.jpcc.0c02944
J. Phys. Chem. C 2020, 124, 15500−15510

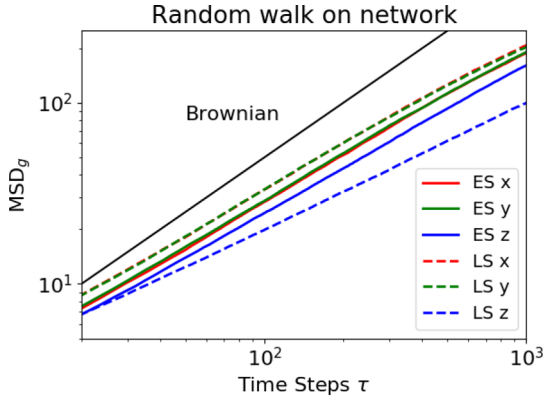

Figure 7. MSD (in reduced units, i.e., particle diameter squared) along x, y, and z directions from a random walk along the network graph corresponding to simulated structures from ES and LS potentials at ϕ = 25%. The black line indicates what purely Brownian motion would be, and MSD$_g$ is found to be sub-diffusive. Because of the inherently anisotropic way in which the network is created, one expects and finds the displacement along z to differ from x and y. Notably, this difference and thus the underlying anisotropy of the network are enhanced for LS, where MSD$_g \propto \tau^{0.7}$ for the z direction instead of $\tau^{0.8}$ as in the other directions.

difference is far more pronounced with the LS potential, demonstrating that the anisotropy in the particle insertion has been built into the network topology. Just as important is the observation that, although there is some shift, the z displacement with ES still closely mirrors x and y. The homogenization of stresses and ordering is coupled to an erasure of the underlying anisotropy.

Porosity. Having characterized the solid network in terms of its percolation, internal stresses, and anisotropy, it is important to understand their implications on the associated pore network. The size, shape, and connectedness of pores not only directly affect the compressive strength but also the long-term stability and resistance to fracture of cement. Additionally, the permeability of the pore network is crucial to the continued reaction of water and cement. Without this, the reaction area would be completely blocked off early in the hydration and stop the reaction.

To start, we compute the pore size distribution (PSD). This is generated using the method of Bhattacharya and Gubbins.[37] It consists of constructing a finite grid, taking points in the pore space, and determining the largest possible radius of a sphere that can fit there without overlapping any particles. This sphere is not necessarily centered at the grid point: Shor's r-algorithm is used to find a local maximum for the radius of a nonoverlapping sphere, constrained to include the selected grid point. From this calculation, we generate the pore frequency $p(s)$, which indicates the fraction p of the total pore space that corresponds to pores of size s. It is to be noted that this method does not provide the shape of the pores: what we obtain corresponds to the smallest linear size of the pore.

The left panel of Figure 8 shows the full PSD with the ES potential (PSD for LS potential in the Supporting Information). We see that the peak pore size is fixed after percolation, maintaining the permeability of the network. The increasing frequency at s = 0.5 nm corresponds to the packing of spherical particles in high-density regions. There is no such clear trend for the LS PSD, and we must separate the edge and center regions to understand what is happening. In the right panel of Figure 8, we plot the first moment of the PSD for both potentials, separated into edge and center regions, as a function of volume fraction.

Looking at the ES results through this new lens, we see that there is a difference in the porosity across the system. At ϕ = 25%, the ≈10% local difference in volume fraction between the edge and center leads to the pores at the edge being a bit smaller. However, relatively speaking, the density difference and consequently the pore size difference are not very large with the ES system. On the other hand, the LS system shows a remarkable transformation after percolation. The edge pores rapidly close up—just as the edge ϕ shoots up dramatically (see Figure 2)—while almost paradoxically the central pore sizes start to increase with the increasing particle number. This is consistent with the coarsening of the initial structure, which would lead to two separated dense C−S−H layers near the system edges. This heterogeneous pore formation has consequences for diffusion through the pores, which can be quantified by performing a random walk in the pore space.

This random walk can be thought of as the trajectory of a particle diffusing through the pores, and in Figure 9, we plot the corresponding mean square displacement (MSD). When split into x, y, and z components, the data show that the pore network tortuosity is isotropic for ES but not for LS. With LS, the x and y components are comparable to the porosity of ES, but the z direction displays a higher tortuosity—indicating reduced diffusivity through the pores. As the cement grain surfaces are modeled to be along this z direction, the diffusion is necessary for the continuation of cement hydration. The

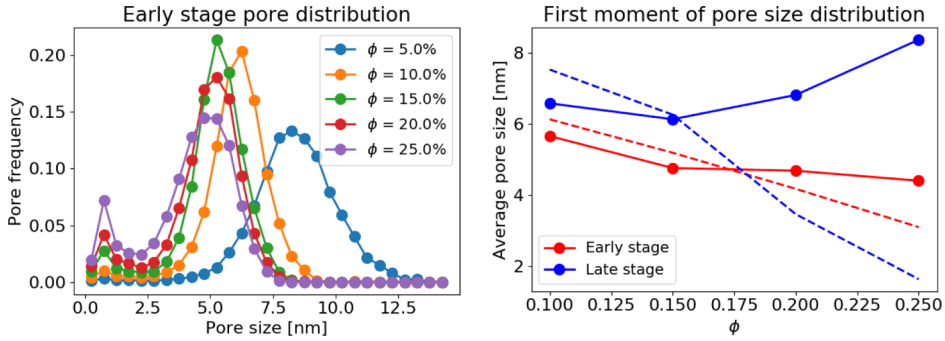

Figure 8. Left: PSD with ES potential for several volume fractions. The pore frequency describes what fraction of pore space is occupied by pores of a given radius. Right: First moment of the PSD for both potentials as a function of ϕ. The solid line represents the low μ middle region, while the dashed line is for the high μ edge.

https://dx.doi.org/10.1021/acs.jpcc.0c02944
J. Phys. Chem. C 2020, 124, 15500−15510

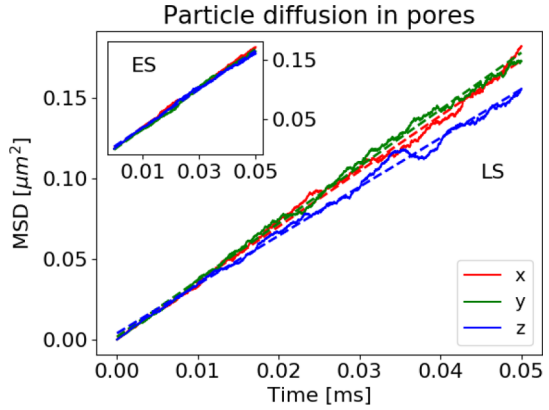

Figure 9. Diffusion through the pore space of the structures corresponding to the two potentials at ϕ = 25%. This is computed from a random walk in the pore space. Assuming that a particle following this random trajectory moves at some fixed speed, one can obtain the overall displacement with time. In an isotropic pore network, this displacement would be evenly split between *x*, *y*, and *z* directions—as in the ES case. For LS, however, there is a decreased displacement along the *z* direction, indicating an increased tortuosity of the pores along the *z* direction.

premature closure of pores could prevent a sufficient degree of hydration being reached.

Specific Surface Area. Experimentally, the porosity of cement pastes can be characterized in terms of the specific surface area, S_{sp}, which is defined as the total surface area of all pores per unit mass. This is probed by scattering experiments or by measuring the ability of the material to uptake gases such as nitrogen or water vapor into pores. From our simulations, it is possible to calculate S_{sp} through the statistics of the pores. In particular, we first compute the pore chord length distribution, that is, the distribution of lengths l_p that randomly drawn chords can traverse in the pore space without intersecting a particle. Our results for ϕ = 25% (Figure 10) show that the

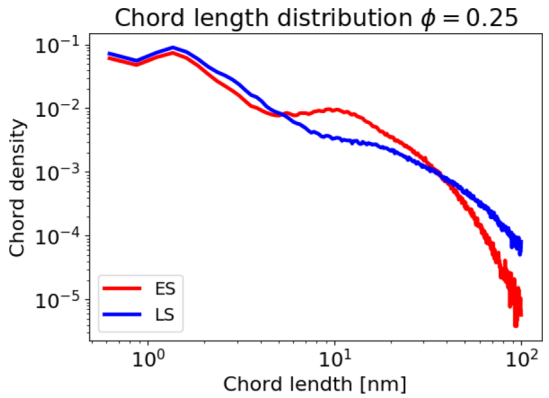

Figure 10. Chord length distribution shows the length of chords drawn randomly in the pore space. The results with ES show a more pronounced peak at intermediate sizes due to the well-controlled pore size.

chord length distribution $p(l_p)$ for ES exhibits a local peak at l_p = 10 nm, consistent with the data in the PSD (peaked at pore radius *s* = 5 nm) of Figure 8 and demonstrating that there is a characteristic size associated with the porosity for ES—a feature that is less pronounced for LS. The repulsive barrier in the two potentials introduces a length scale to our system which affects the porosity, and the strength of that barrier controls how important this length scale is.

From the mean of the chord length distribution $\langle l_p \rangle$, we calculate the specific surface area S_{sp} of our system using, according to refs 38 and 39:

$$S_{sp} = \frac{4(1-\phi)}{\rho\phi\langle l_p \rangle} \tag{5}$$

where ρ is the density of the C−S−H matrix, which is estimated to be 2.43 g/cm^3 from atomistic simulations.[2,3] Because of the discrete nature of numerical calculations, the chord length distribution is computed with a finite cutoff l_c, which affects the value of S_{sp}. To obtain the true surface area, one can calculate this by varying l_c and extrapolating to the l_c = 0 limit (Figure 11, left).

The specific surface area computed depends on l_c differently for the two potentials. This is something that needs to be considered when trying to compare with experimental data. Interestingly, despite the clearly different nature of the porosity for ES and LS, we actually end up with quite similar overall specific surface area (Figure 11, right). However, in comparison with experiments, we must be careful of these different features and try to understand which parts of the porosity an experiment will be able to access. These limitations will apply differently to the two gel morphologies corresponding to ES and LS.

The values reported for S_{sp} of hardened cement paste using the gas sorption experiments vary in the range of approximately 50−200 m^2/g.[4,9,12,40,41] Meanwhile, mesoscale simulations[21] have reported values of S_{sp} = 347 m^2/g and S_{sp} = 283 m^2/g for ϕ = 33% and ϕ = 52%, respectively. Our results are clearly significantly higher than these values, plateauing around S_{sp} = 600 m^2/g at ϕ = 25%. However, given that S_{sp} decreases with increasing ϕ that is expected, at the very early stages of hydration, to which our simulations correspond, experimental measurements are challenging because of how rapidly the material changes. Additionally, there is a significant quantity of unreacted cement at this stage, skewing possible experimental results in comparison to our simulations (which do not explicitly contain cement grains). A study by Suda et al. suggests that the specific surface area associated with C−S−H only is closer to 200−300 m^2/g.[42] Finally, one should keep in mind that no matter how sensitive, sorption techniques only access well-connected pores of the sufficient size. If we take a larger l_c such that only pores of diameter greater than 3 nm are considered, S_{sp} falls to be about 300 m^2/g. Alternatively, if we look at results from more sensitive small angle X-ray scattering experiments, the values of S_{sp} > 500 m^2/g have been reported.[4,43]

Scattering. In addition to measuring the specific surface area, neutron and X-ray scattering experiments have been used to characterize the microstructure of cement pastes—and are one of the most powerful tools to do so. The usual way to compute $I(\vec{q})$ is as the Fourier transform of the autocorrelation of fluctuations in local density, $\eta_2(\vec{r}) = \frac{1}{V}\int d^3r'(\rho(\vec{r'}) - \bar{\rho})(\rho(\vec{r'} + \vec{r}) - \bar{\rho})$, of our simulated microstructures (Figure 12), where $\rho(\vec{r})$ is the local density and $\bar{\rho}$ the average density.[44] In case of an anisotropic medium, this computation is more involved because of the need to compute $\eta_2(\vec{r})$ for each orientation of $\vec{r}$ prior to performing the 3D Fourier transform.

https://dx.doi.org/10.1021/acs.jpcc.0c02944
J. Phys. Chem. C 2020, 124, 15500−15510

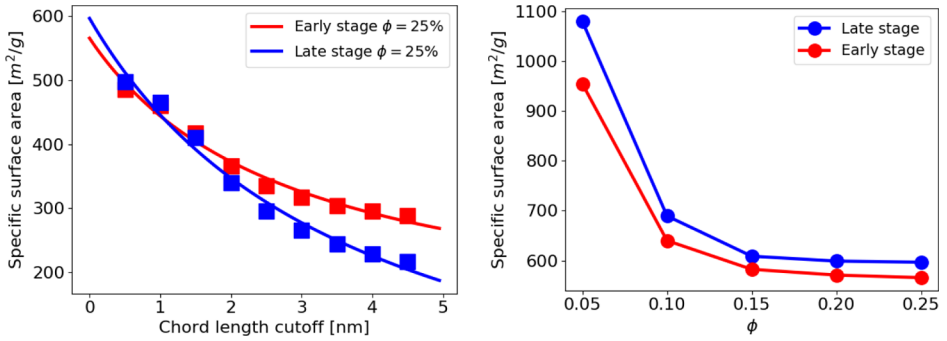

Figure 11. Left: The specific surface area as a function of the chosen chord length cutoff. By fitting the calculated data points to $f(l_c) = \frac{A}{1 + Bl_c} + C$, we extrapolate to the $l_c = 0$ limit and obtain the geometric surface area $S_{sp} = A + C$. Right: The value for the specific surface area obtained by extrapolation for different volume fraction ϕ.

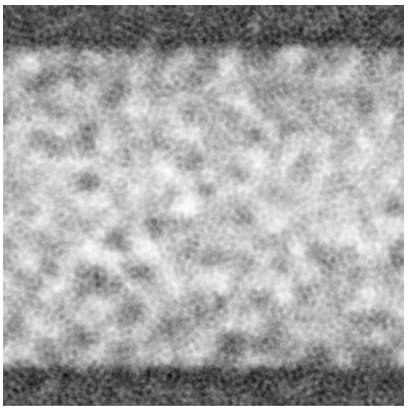

Figure 12. 2D projection of local densities in the LS structure at ϕ = 25% when looking down the y-axis. The darker regions correspond to higher density. Scattering intensity $I(q)$ can be computed from the autocorrelation of fluctuations in the local density, $\eta_2(r)$.

A second way, more numerical tractable, was proposed in refs 45 and 46. This a two-step process. First, a projection image of the chosen 3D binary structure is performed either along the x or y or z direction. Second, a 2D Fourier transform of this projection is calculated. The associated spectral density gives directly $I(q_x, q_y, q_z)$ with either $q_x = 0$ or $q_y = 0$ or $q_z = 0$. For example, the projection along the optical axis x will allow one to get the 2D pattern $I(q_x = 0, q_y, q_z)$. To estimate the level of anisotropy, an angular average along the principal directions of these 2D scattering patterns is performed using an averaging angle of 15°. A comparison of the two methods is presented in ref 46, showing a very good agreement.

Because of the anisotropy in the structure, the choice of optical axis for the scattering naturally affects the results obtained. Because of the symmetries in our system, the x and y directions are equivalent—anisotropy is associated with the z direction, that is, the μ-gradient direction. If one considers an optical direction along a non-z axis, the μ and density gradients produce clear differences in the low q scattering intensity along the z direction compared to the x or y direction (Figure 13). For both ES and LS potentials, the scattering along z exhibits a low q structure (instead of a plateau as along x or y direction), which is consistent with the system-spanning density gradient along z direction. The high q scattering is instead dominated by the oscillations typical of monodispersed spherical particles.[47]

One can also consider just the scattering from the center region of the system (green triangles in Figure 13). Limiting ourselves to this region reveals an interesting difference between the two potentials. With LS, the z scattering deviates from y scattering in the low μ center region as well—highlighting that the anisotropy in the structure goes beyond the large difference in density, stresses, porosity, and so forth between the edge and center regions. On the other hand, for ES, this split leads to a suppression of scattering anisotropy and produces a curve which matches the scattering along x. This

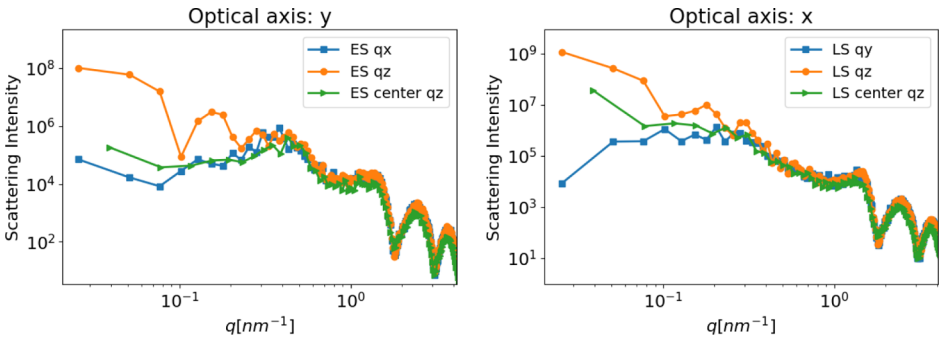

Figure 13. Scattering intensity computed for both potentials for various different optical axes. The intensity is split into components along different directions to highlight anisotropy. The scattering component along z differs from the others at low q because of anisotropy in the structure. Surprisingly, for ES, this effect is suppressed if we consider only the center region—meaning all of the measured anisotropy is due to the density variation across the whole box. Meanwhile, for LS, even the center region alone deviates from the x and y scattering. The structure is anisotropic even at scales smaller than the system-wide μ gradient. The high q oscillations are consistent with having monodispersed spherical particles.

https://dx.doi.org/10.1021/acs.jpcc.0c02944
J. Phys. Chem. C 2020, 124, 15500−15510

suggests that the anisotropy is due entirely to the differences between the high and low μ regions.

The anisotropy induced by the cement grain surfaces manifests itself in our calculated scattering intensity. For a macroscopic sample, these grains would be distributed randomly and give an overall isotropic response because of the statistical averaging of the results. The isotropic $I(q)$ has been computed using similar mesoscale models for high volume fractions,[21] and it was found to match experimental measurements of scattering intensity. It is difficult to make such a connection using our simulations because of limitations of the system size at low q and the effects of particle size monodispersity at high q. Nonetheless, this calculation has revealed interesting differences in the anisotropy of ES and LS systems. Future studies can expand on this to make a direct connection to scattering experiments.

CONCLUSIONS

We used MD and GCMC simulations to investigate the effect of C−S−H growth in the presence of spatial gradients of C−S−H precipitation and of the changing effective interactions between C−S−H nanoparticles on the overall morphology of the C−S−H gel. Using GCMC to mimic precipitation of nanoparticles, we observed how the precipitation at cement grain surfaces leads to spatial gradients in density which develop over time but depend on the features of the C−S−H interactions. With the ES interaction, we discovered a percolating cluster that forms around ϕ = 15% with reduced density and stress gradients, as well as network anisotropy, relative to the LS interaction. Calculations of pore size and diffusion in the pores demonstrated that these differences in the gel morphology translated into coarsening pores and an increase in pore tortuosity along the gradient direction for the LS system. Finally, we computed the specific surface area and scattering intensity to make a connection to experimental methods of characterizing the cement microstructure.

The heterogeneous growth of C−S−H nanoparticles clearly has an effect on the morphology of the gel that is formed, and this effect of spatial gradients in the C−S−H precipitation is controlled by the features of the interaction potential between the C−S−H nanoparticles. The noncontact repulsion that is present in early stages of hydration because of electrostatics plays a crucial role in the formation of a percolated and stress-bearing network with limited anisotropy. It also helps prevent the formation of large pores because of coarsening while maintaining diffusivity in the pores. These features are necessary to the continuing hydration of cement grains and the formation of a connected solid structure. As the interactions evolve over time, the presence of the cement grain surfaces can drive the formation of spatial gradients in C−S−H density and differences in local packing and density—consistent with the two distinct morphological phases of C−S−H observed in the literature.[33,34]

Our study provides further support to the idea proposed by Ioannidou et al.: the natural time evolution of the interaction between C−S−H nanoparticles is crucial to attaining the final mechanical strength through complex tuning of the gel morphology.[20] Under spatial gradients of C−S−H precipitation, the differences in gel morphology due to the interactions are not only maintained but also enhanced. In the context of heterogeneous C−S−H nucleation, the features of the early stage interactions are required to explain how cement setting can be such a complex but robust process. These discoveries give insight into how the growth of nanoscale components builds up the overall microstructure of cement hydrates and how it depends on the interactions between the nanoparticles. Such an insight is an important step toward understanding how an alternative cementitious material could behave through the changes in chemistry and thus the effective interactions.

ASSOCIATED CONTENT

Supporting Information

The Supporting Information is available free of charge at https://pubs.acs.org/doi/10.1021/acs.jpcc.0c02944.

Local ordering and signatures of locally crystalline or Bernal spiral-like structures. Full PSDs for both potentials (PDF)

AUTHOR INFORMATION

Corresponding Author

Emanuela Del Gado − *Department of Physics, Institute for Soft Matter Synthesis and Metrology, Georgetown University, Washington, D.C. 20057, United States;* orcid.org/0000-0002-8340-0290; Email: ed610@georgetown.edu

Authors

Abhay Goyal − *Department of Physics, Institute for Soft Matter Synthesis and Metrology, Georgetown University, Washington, D.C. 20057, United States;* orcid.org/0000-0002-0587-2145

Katerina Ioannidou − *Laboratoire de Mécanique et Génie Civil, CNRS, Université de Montpellier, Montpellier 34090, France; Massachusetts Institute of Technology/CNRS/Aix-Marseille University Joint Laboratory, Cambridge, Massachusetts 02139, United States; Department of Civil and Environmental Engineering, Massachusetts Institute of Technology, Cambridge, Massachusetts 02139, United States*

Christopher Tiede − *Department of Physics, Institute for Soft Matter Synthesis and Metrology, Georgetown University, Washington, D.C. 20057, United States*

Pierre Levitz − *Physico-Chimie des Électrolytes et Nanosystèmes Interfaciaux, PHENIX, Sorbonne Université, CNRS, F-75005 Paris, France*

Roland J.-M. Pellenq − *Massachusetts Institute of Technology/CNRS/Aix-Marseille University Joint Laboratory, Cambridge, Massachusetts 02139, United States; Department of Civil and Environmental Engineering, Massachusetts Institute of Technology, Cambridge, Massachusetts 02139, United States; Department of Physics, Institute for Soft Matter Synthesis and Metrology, Georgetown University, Washington, D.C. 20057, United States;* orcid.org/0000-0001-5559-4190

Complete contact information is available at: https://pubs.acs.org/10.1021/acs.jpcc.0c02944

Notes

The authors declare no competing financial interest.

ACKNOWLEDGMENTS

A.G. and E.D.G. acknowledge the NIST PREP Gaithersburg Program (70NANB18H151) and Georgetown University for support.

REFERENCES

(1) Allen, A. J.; Thomas, J. J.; Jennings, H. M. Composition and density of nanoscale calciumsilicatehydrate in cement. *Nat. Mater.* **2007**, *6*, 311−316.

(2) Qomi, M. J. A.; Krakowiak, K. J.; Bauchy, M.; Stewart, K. L.; Shahsavari, R.; Jagannathan, D.; Brommer, D. B.; Baronnet, A.; Buehler, M. J.; Yip, S.; et al. Combinatorial molecular optimization of cement hydrates. *Nat. Commun.* **2014**, *5*, 4960.

(3) Pellenq, R. J.-M.; Kushima, A.; Shahsavari, R.; Van Vliet, K. J.; Buehler, M. J.; Yip, S.; Ulm, F.-J. A realistic molecular model of cement hydrates. *Proc. Natl. Acad. Sci. U.S.A.* **2009**, *106*, 16102−16107.

(4) Thomas, J. J.; Jennings, H. M.; Allen, A. J. The surface area of hardened cement paste as measured by various techniques. *Concr. Sci. Eng.* **1999**, *1*, 45−64.

(5) Ranaivomanana, H.; Verdier, J.; Sellier, A.; Bourbon, X. Toward a better comprehension and modeling of hysteresis cycles in the water sorption-desorption process for cement based materials. *Cem. Concr. Res.* **2011**, *41*, 817−827.

(6) Andrew, R. M. Global CO2 emissions from cement production. *Earth Syst. Sci. Data* **2018**, *10*, 2213.

(7) Flatt, R. J.; Roussel, N.; Cheeseman, C. R. Concrete: An eco material that needs to be improved. *J. Eur. Ceram. Soc.* **2012**, *32*, 2787−2798.

(8) Bullard, J. W.; Jennings, H. M.; Livingston, R. A.; Nonat, A.; Scherer, G. W.; Schweitzer, J. S.; Scrivener, K. L.; Thomas, J. J. Mechanisms of cement hydration. *Cem. Concr. Res.* **2011**, *41*, 1208−1223.

(9) Taylor, H. *Cement Chemistry*; Thomas Telford: London, 1997.

(10) Pustovgar, E.; Sangodkar, R. P.; Andreev, A. S.; Palacios, M.; Chmelka, B. F.; Flatt, R. J.; d'Espinose de Lacaillerie, J.-B. Understanding silicate hydration from quantitative analyses of hydrating tricalcium silicates. *Nat. Commun.* **2016**, *7*, 10952.

(11) Lootens, D.; Hébraud, P.; Lécolier, E.; Van Damme, H. Gelation, shear-thinning and shear-thickening in cement slurries. *Oil Gas Sci. Technol.* **2004**, *59*, 31−40.

(12) Thomas, J. J.; Jennings, H. M.; Allen, A. J. the Surface Area of Cement Paste As Measured By Neutron. *Cem. Concr. Res.* **1998**, *28*, 897−905.

(13) Chiang, W.-S.; Fratini, E.; Baglioni, P.; Liu, D.; Chen, S.-H. Microstructure determination of calcium-silicate-hydrate globules by small-angle neutron scattering. *J. Phys. Chem. C* **2012**, *116*, 5055−5061.

(14) Vandamme, M.; Ulm, F.-J. Nanogranular origin of concrete creep. *Proc. Natl. Acad. Sci. U.S.A.* **2009**, *106*, 10552−10557.

(15) Mondal, P.; Shah, S. P.; Marks, L. D. Nanoscale characterization of cementitious materials. *ACI Mater. J.* **2008**, *105*, 174−179.

(16) Thomas, J. J.; Jennings, H. M.; Chen, J. J. Influence of nucleation seeding on the hydration mechanisms of tricalcium silicate and cement. *J. Phys. Chem. C* **2009**, *113*, 4327−4334.

(17) Garrault, S.; Finot, E.; Lesniewska, E.; Nonat, A. Study of C-S-H growth on C3S surface during its early hydration. *Mater. Struct.* **2005**, *38*, 435−442.

(18) Plassard, C.; Lesniewska, E.; Pochard, I.; Nonat, A. Nanoscale Experimental Investigation of Particle Interactions at the Origin of the Cohesion of Cement. *Langmuir* **2005**, *21*, 7263−7270.

(19) Lesko, S.; Lesniewska, E.; Nonat, A.; Mutin, J.-C.; Goudonnet, J.-P. Investigation by atomic force microscopy of forces at the origin of cement cohesion. *Ultramicroscopy* **2001**, *86*, 11−21.

(20) Ioannidou, K.; Kanduč, M.; Li, L.; Frenkel, D.; Dobnikar, J.; Del Gado, E. The crucial effect of early-stage gelation on the mechanical properties of cement hydrates. *Nat. Commun.* **2016**, *7*, 12106.

(21) Ioannidou, K.; Krakowiak, K. J.; Bauchy, M.; Hoover, C. G.; Masoero, E.; Yip, S.; Ulm, F.-J.; Levitz, P.; Pellenq, R. J.-M.; Del Gado, E. Mesoscale texture of cement hydrates. *Proc. Natl. Acad. Sci. U.S.A.* **2016**, *113*, 2029−2034.

(22) Pellenq, R. J.-M.; Van Damme, H. Why Does Concrete Set?: The Nature of Cohesion Forces in Hardened Cement-Based Materials. *MRS Bull.* **2004**, *29*, 319−323.

(23) Jönsson, B.; Wennerström, H.; Nonat, A.; Cabane, B. Onset of cohesion in cement paste. *Langmuir* **2004**, *20*, 6702−6709.

(24) Jönsson, B.; Nonat, A.; Labbez, C.; Cabane, B.; Wennerström, H. Controlling the Cohesion of Cement Paste. *Langmuir* **2005**, *21*, 9211−9221.

(25) Bonnaud, P. A.; Labbez, C.; Miura, R.; Suzuki, A.; Miyamoto, N.; Hatakeyama, N.; Miyamoto, A.; Van Vliet, K. J. Interaction grand potential between calciumsilicatehydrate nanoparticles at the molecular level. *Nanoscale* **2016**, *8*, 4160−4172.

(26) Masoumi, S.; Valipour, H.; Abdolhosseini Qomi, M. J. Intermolecular Forces between Nanolayers of Crystalline Calcium-Silicate-Hydrates in Aqueous Medium. *J. Phys. Chem. C* **2017**, *121*, 5565−5572.

(27) Ciach, A.; Pękalski, J.; Góźdź, W. T. Origin of similarity of phase diagrams in amphiphilic and colloidal systems with competing interactions. *Soft Matter* **2013**, *9*, 6301.

(28) Zhuang, Y.; Zhang, K.; Charbonneau, P. Equilibrium Phase Behavior of a Continuous-Space Microphase Former. *Phys. Rev. Lett.* **2016**, *116*, 098301.

(29) Frenkel, D.; Smit, B. *Understanding Molecular Simulation*, 2nd ed.; Academic Press: San Diego, 2002.

(30) Widom, B. Some Topics in the Theory of Fluids. *J. Chem. Phys.* **1963**, *39*, 2808−2812.

(31) Ioannidou, K.; Pellenq, R. J.-M.; Del Gado, E. Controlling local packing and growth in calciumsilicatehydrate gels. *Soft Matter* **2014**, *10*, 1121−1133.

(32) Plimpton, S. Fast Parallel Algorithms for Short Range Molecular Dynamics. *J. Comput. Phys.* **1995**, *117*, 1−19.

(33) Tennis, P. D.; Jennings, H. M. Model for two types of calcium silicate hydrate in the microstructure of Portland cement pastes. *Cem. Concr. Res.* **2000**, *30*, 855−863.

(34) Constantinides, G.; Ulm, F.-J. The effect of two types of C-S-H on the elasticity of cement-based materials: Results from nano-indentation and micromechanical modeling. *Cem. Concr. Res.* **2004**, *34*, 67−80.

(35) Bae, S.; Kanematsu, M.; Hernández-Cruz, D.; Moon, J.; Kilcoyne, D.; Monteiro, P. J. In situ soft X-ray spectromicroscopy of early tricalcium silicate hydration. *Materials* **2016**, *9*, 976.

(36) Thompson, A. P.; Plimpton, S. J.; Mattson, W. General formulation of pressure and stress tensor for arbitrary many-body interaction potentials under periodic boundary conditions. *J. Chem. Phys.* **2009**, *131*, 154107.

(37) Bhattacharya, S.; Gubbins, K. E. Fast method for computing pore size distributions of model materials. *Langmuir* **2006**, *22*, 7726−7731.

(38) Levitz, P.; Tchoubar, D. Disordered porous solids : from chord distributions to small angle scattering. *J. Phys. I* **1992**, *2*, 771−790.

(39) Pellenq, R. J.-M.; Levitz, P. E. Capillary condensation in a disordered mesoporous medium: a grand canonical Monte Carlo study. *Mol. Phys.* **2002**, *100*, 2059−2077.

(40) Mikhail, R. S.; Copeland, L. E.; Brunauer, S. Pore structures and surface areas of hardened portland cement pastes by Nitrogen adsorption. *Can. J. Chem.* **1964**, *42*, 426−438.

(41) Baroghel-Bouny, V.; Mainguy, M.; Lassabatere, T.; Coussy, O. Characterization and identification of equilibrium and transfer moisture properties for ordinary and high-performance cementitious materials. *Cem. Concr. Res.* **1999**, *29*, 1225−1238.

(42) Suda, Y.; Saeki, T.; Saito, T. Relation between chemical composition and physical properties of C-S-H generated from cementitious materials. *J. Adv. Concr. Technol.* **2015**, *13*, 275−290.

(43) Winslow, D. N.; Bukowski, J. M.; Francis Young, J. The early evolution of the surface of hydrating cement. *Cem. Concr. Res.* **1994**, *24*, 1025−1032.

(44) Brisard, S.; Levitz, P. Small-angle scattering of dense, polydisperse granular porous media: Computation free of size effects. *Phys. Rev. E: Stat., Nonlinear, Soft Matter Phys.* **2013**, *87*, 013305.

https://dx.doi.org/10.1021/acs.jpcc.0c02944
J. Phys. Chem. C 2020, 124, 15500−15510

(45) Brisard, S.; Chae, R. S.; Bihannic, I.; Michot, L.; Guttmann, P.; Thieme, J.; Schneider, G.; Monteiro, P. J. M.; Levitz, P. Morphological quantification of hierarchical geomaterials by X-ray nano-CT bridges the gap from nano to micro length scales. *Am. Mineral.* **2012**, *97*, 480−483.
(46) Ferrage, E.; Hubert, F.; Baronnet, A.; Grauby, O.; Tertre, E.; Delville, A.; Bihannic, I.; Prêt, D.; Michot, L. J.; Levitz, P. Influence of crystal structure defects on the small-angle neutron scattering/diffraction patterns of clay-rich porous media. *J. Appl. Crystallogr.* **2018**, *51*, 1311−1322.
(47) Guinier, A.; Fournet, G. *Small-Angle Scattering of X-rays*; Wiley: New York, 1955.

https://dx.doi.org/10.1021/acs.jpcc.0c02944
J. Phys. Chem. C 2020, 124, 15500−15510